# GPU accelerated study of a dual-frequency driven single bubble in a 6-dimensional parameter space: the active cavitation threshold

Ferenc Hegedűs[a,*], Kálmán Klapcsik[a], Werner Lauterborn[b], Ulrich Parlitz[c], Robert Mettin[b]

[a] *Department of Hydrodynamic Systems, Faculty of Mechanical Engineering, Budapest University of Technology and Economics, Budapest, Hungary*

[b] *Drittes Physikalisches Institut, Georg-August-Universität Göttingen, Göttingen, Germany*

[c] *Research Group Biomedical Physics, Max Planck Institute for Dynamics and Self-Organization and Institut für Dynamik komplexer Systeme, Georg-August-Universität Göttingen, Göttingen, Germany*

**Abstract**

The active cavitation threshold of a dual-frequency driven single spherical gas bubble is studied numerically. This threshold is defined as the minimum energy required to generate a given relative expansion $(R_{max} - R_E)/R_E$, where $R_E$ is the equilibrium size of the bubble and $R_{max}$ is the maximum bubble radius during its oscillation. The model employed is the Keller–Miksis equation that is a second order ordinary differential equation. The parameter space investigated is composed by the pressure amplitudes, excitation frequencies, phase shift between the two harmonic components and by the equilibrium bubble radius (bubble size). Due to the large 6-dimensional parameter space, the number of the parameter combinations investigated is approximately two billion. Therefore, the high performance of graphics processing units is exploited; our in-house code is written in C++ and CUDA C software environments. The results show that for $(R_{max} - R_E)/R_E = 2$, the best choice of the frequency pairs depends on the bubble size. For small bubbles, below 3 $\mu$m, the best option is to use equal frequencies and low ones in the giant response region. For medium sized bubbles, between 3 $\mu$m and 6 $\mu$m, the optimal choice is the mixture of low frequency (giant response) and main resonance frequency. For large bubbles, above 6 $\mu$m, the main resonance dominates the active cavitation threshold. Increasing the prescribed relative expansion value to $(R_{max} - R_E)/R_E = 3$, the optimal choice is always equal frequencies with the lowest values (20 kHz here). Thus, in this case, the giant response always dominates the active cavitation threshold. The phase shift between the harmonic components of the driving has no effect on the threshold.

*Keywords:* Keller–Miksis equation, bubble dynamics, dual-frequency driving, cavitation threshold, GPU programming

*Corresponding author

*Email addresses:* `fhegedus@hds.bme.hu` (Ferenc Hegedűs), `kklapcsik@hds.bme.hu` (Kálmán Klapcsik), `werner.lauterborn@phys.uni-goettingen.de` (Werner Lauterborn), `ulrich.parlitz@ds.mpg.de` (Ulrich Parlitz), `robert.mettin@phys.uni-goettingen.de` ( Robert Mettin)

## 1. Introduction

Sonochemistry is a special branch of chemistry which intends to produce chemical species via the irradiation of a liquid with ultrasound [1–7]. Due to the high amplitude pressure waves, bubble clusters are formed in the liquid domain composed of nearly spherical bubbles [8–18]. During their radial pulsation, the high compression ratio might result in thousands of degrees of Kelvin internal temperature inducing chemical reactions [19–24]. Some of the interests of sonochemical applications are the production of hydrogen (green fuel) [25–28], free radicals for wastewater treatment [29–32] or nanoalloys/nanoparticles which are efficient catalysts [33–35].

Several experimental results have shown that the application of dual-frequency irradiation can increase the sonochemical yield significantly (even by 300%) compared to the conventional single frequency case [36–48]. These studies reported that the chemical yield of dual-frequency irradiation is usually higher than the sum of the chemical yields of single frequency sonications. This indicates that there is a synergetic effect between the harmonic components. During the last decades, many theories have been devised to explain this effect: better pattern of the pressure waves inside a sonochemical reactor (e.g. more active zones) [43, 49–51], more cavitation nuclei are generated for feeding the bubble clusters [44, 50–52], increased mass transfer via micromixing [50, 53] or the increased collapse strength of the individual bubbles [39, 41].

Still, the theoretical background of the synergetic effect is unclear. Moreover, reports on decreased sonochemical efficiency of dual-frequency irradiation were also published, see e.g. [53]. Many researchers investigated dual-frequency driven single bubbles [54–57] to find evidence for the synergetic effect of this approach and to establish a theory through the investigation of the dynamics of a single spherical bubble. For example, the form of the signal of the external dual-frequency driving (e.g., bigger difference between its minimum and maximum) can produce bubble dynamics having a stronger collapse [26, 58, 59] or a lower active cavitation threshold [60, 61]. The special resonance properties of the bubble caused by dual-frequency excitation (e.g., combination and simultaneous resonances) can explain the increased cavitational activity [62, 63]. Also, the dual-frequency driving can alter the spherical stability threshold [64] or increase the mass transfer through the bubble interface [65]. The present study focuses on the reduction of the active cavitation threshold, which is usually defined as how much input energy is required (formulated in terms of the pressure amplitudes) to obtain a cavitationally active bubble dynamics. However, in our opinion the results in the literature are not exhaustive enough. The main reason is the large number of parameters involved when using multi-frequency driving. Even in case of a dual-frequency driving, the minimum number of parameters that needs to be investigated is six: two pressure amplitudes, two frequencies, the phase shift between the harmonic components and the bubble size. Therefore, the limited number of investigated parameter combinations in the literature can hide their complex impact on the bubble dynamics.

In this sense, the main aim of the present study is to perform high-resolution scans in the 6-dimensional parameter space by exploiting the large processing power of graphics processing units (GPUs). Even with a careful planning of the parameter ranges and their resolution, the total number of parameter combinations is approximately 2 billion, for details see Sec. 3. Such a detailed investigation may help to identify the synergetic effect between the harmonic components of the driving. The employed model is the Keller–

Miksis equation that is a second order ordinary differential equation. It is used due to its simplicity as the number of parameter combinations is quite large. The solver used is based on our in-house code written in C++ and CUDA C, and it is free to use under an MIT license. The interested reader is referred to the website [66] of the program package or to its GitHub repository [67]. The software package also has a detailed manual with tutorial examples [68].

Beyond the scope of sonochemistry, the results obtained on dual-frequency driven single bubble can have a significant impact on other specialised fields of acoustic cavitation. For instance, dual-frequency driving is successfully used in therapeutic applications to decrease the active cavitation threshold [40] and to minimise the damage and mental stress to the patients [69, 70]. In diagnostic ultrasound, it is widely used to enhance the contrast of ultrasound (subharmonic) imaging [71, 72]. Moreover, the dual-frequency technique has importance in bubble sizing [73], boosting sonoluminescence [74] or controlling chaotic oscillations of bubbles [75].

## 2. The bubble model

The governing equation is the Keller–Miksis equation describing the evolution of the radius of a spherical gas bubble placed in a liquid domain and subjected to external excitation [14]. The second-order, ordinary differential equation reads

$$\left(1-\frac{\dot{R}}{c_L}\right)R\ddot{R}+\left(1-\frac{\dot{R}}{3c_L}\right)\frac{3}{2}\dot{R}^2=\left(1+\frac{\dot{R}}{c_L}+\frac{R}{c_L}\frac{d}{dt}\right)\frac{(p_L-p_\infty(t))}{\rho_L}, \tag{1}$$

where $R(t)$ is the time dependent bubble radius; $c_L = 1497.3\,\mathrm{m/s}$ and $\rho_L = 997.1\,\mathrm{kg/m^3}$ are the sound speed and density of the liquid domain, respectively. The pressure far away from the bubble, $p_\infty(t)$, is composed by static and by periodic components

$$p_\infty(t) = P_\infty + P_{A1}\sin(\omega_1 t) + P_{A2}\sin(\omega_2 t+\theta), \tag{2}$$

where $P_\infty = 1\,\mathrm{bar}$ is the ambient pressure. The periodic components have pressure amplitudes $P_{A1}$ and $P_{A2}$, angular frequencies $\omega_1 = 2\pi f_1$ and $\omega_2 = 2\pi f_2$, and a phase shift $\theta$.

The connection between the pressures inside and outside the bubble at its interface is chosen as

$$p_G + p_V = p_L + \frac{2\sigma}{R} + 4\mu_L\frac{\dot{R}}{R}, \tag{3}$$

where the total pressure inside the bubble is the sum of the partial pressures of the non-condensable gas, $p_G$, and the vapour, $p_V = 3166.8\,\mathrm{Pa}$. Thermal effects and mass transfer are not taken into account. The surface tension is $\sigma = 0.072\,\mathrm{N/m}$ and the liquid kinematic viscosity is $\mu_L = 8.902^{-4}\,\mathrm{Pa\,s}$. The gas inside the bubble is assumed to obey a simple polytropic relationship

$$p_G = \left(P_\infty - p_V + \frac{2\sigma}{R_E}\right)\left(\frac{R_E}{R}\right)^{3\gamma}, \tag{4}$$

where the polytropic exponent $\gamma$ for air is chosen ($\gamma = 1.4$, adiabatic behaviour) and the equilibrium bubble radius is $R_E$.

System (1)-(4) is transformed into a dimensionless form by the introduction of the following dimensionless variables

$$\tau = \frac{\omega_1}{2\pi} t, \tag{5}$$

$$y_1 = \frac{R}{R_E}, \tag{6}$$

$$y_2 = \dot{R} \frac{2\pi}{R_E \omega_1}. \tag{7}$$

The dimensionless system is written as

$$\dot{y}_1 = y_2, \tag{8}$$

$$\dot{y}_2 = \frac{N_{\mathrm{KM}}}{D_{\mathrm{KM}}}, \tag{9}$$

where the numerator, $N_{\mathrm{KM}}$, and the denominator, $D_{\mathrm{KM}}$, are

$$\begin{aligned} N_{\mathrm{KM}} = (C_0 + C_1 y_2) \left( \frac{1}{y_1} \right)^{C_{10}} - C_2 \left(1 + C_9 y_2\right) - C_3 \frac{1}{y_1} - C_4 \frac{y_2}{y_1} - \\ \left(1 - C_9 \frac{y_2}{3}\right) \frac{3}{2} y_2^2 - \left(C_5 \sin(2\pi\tau) + C_6 \sin(2\pi C_{11}\tau + C_{12})\right) \left(1 + C_9 y_2\right) \\ - y_1 \left(C_7 \cos(2\pi\tau) + C_8 \cos(2\pi C_{11}\tau + C_{12})\right), \end{aligned} \tag{10}$$

and

$$D_{\mathrm{KM}} = y_1 - C_9 y_1 y_2 + C_4 C_9, \tag{11}$$

respectively.

The coefficients are summarised as follows:

$$C_0 = \frac{1}{\rho_L}\left(P_\infty - p_V + \frac{2\sigma}{R_E}\right)\left(\frac{2\pi}{R_E\omega_1}\right)^2, \tag{12}$$

$$C_1 = \frac{1-3\gamma}{\rho_L c_L}\left(P_\infty - p_V + \frac{2\sigma}{R_E}\right)\frac{2\pi}{R_E\omega_1}, \tag{13}$$

$$C_2 = \frac{P_\infty - p_V}{\rho_L}\left(\frac{2\pi}{R_E\omega_1}\right)^2, \tag{14}$$

$$C_3 = \frac{2\sigma}{\rho_L R_E}\left(\frac{2\pi}{R_E\omega_1}\right)^2, \tag{15}$$

$$C_4 = \frac{4\mu_L}{\rho_L R_E^2}\frac{2\pi}{\omega_1}, \tag{16}$$

$$C_5 = \frac{P_{A1}}{\rho_L}\left(\frac{2\pi}{R_E\omega_1}\right)^2, \tag{17}$$

$$C_6 = \frac{P_{A2}}{\rho_L}\left(\frac{2\pi}{R_E\omega_1}\right)^2, \tag{18}$$

$$C_7 = R_E\frac{\omega_1 P_{A1}}{\rho_L c_L}\left(\frac{2\pi}{R_E\omega_1}\right)^2, \tag{19}$$

$$C_8 = R_E\frac{\omega_1 P_{A2}}{\rho_L c_L}\left(\frac{2\pi}{R_E\omega_1}\right)^2, \tag{20}$$

$$C_9 = \frac{R_E\omega_1}{2\pi c_L}, \tag{21}$$

$$C_{10} = 3\gamma, \tag{22}$$

$$C_{11} = \frac{\omega_2}{\omega_1}, \tag{23}$$

$$C_{12} = \theta. \tag{24}$$

## 3. The investigated parameter space

Assuming that the liquid ambient properties (temperature and pressure) and the liquid composition are fixed, the main control parameters that affect the bubble dynamics are the properties of the external dual-frequency driving. Therefore, the first five parameters investigated here are the pressure amplitudes $P_{A1}$ and $P_{A2}$, the excitation frequencies $f_1$ and $f_2$ and the phase shift between the harmonic components of the driving $\theta$. In addition, the sixth parameter is the equilibrium bubble radius $R_E$ characterising the size of the bubble since it varies significantly in a sonochemical reactor.

The ranges (minimum and maximum values), resolutions and the type of the distributions (linear or logarithmic) of the six parameters varied are summarised in Tab. 1. That is, the pressure amplitudes are varied between 0 and 2 bar with an increment of 0.1 bar. This means 21 equidistant values of the pressure amplitudes. In order to resolve the different kinds of resonance properties of the system, the resolution of the frequencies (varied between 20 kHz and 2 MHz) is increased to 101. Moreover, a logarithmic scale is applied to resolve the two orders of magnitude difference in the frequency ranges properly. The values of the phase shift are distributed evenly between 0 and $2\pi(1-1/20)$ with a resolution of 20 (taking into account the periodicity property). The bubble size is varied between 1 and 10 $\mu$m with an increment of 0.5 $\mu$m. This covers the typical ranges of bubble sizes observed during experiments [76–79]. Although the employed parameter resolutions can be considered quite moderate, the total number of parameter combinations is approximately 1.89 billion. The overall simulation time was approximately 2 weeks using two Nvidia Tesla P100 graphics cards. This justifies the application of high-performance GPU programming mentioned already in Sec. 1.

Table 1: Ranges, resolutions and the types of distribution of the control parameters of the 6-dimensional parameter space. The abbreviations lin, log, and res stand for linear, logarithmic, and resolution, respectively.

| | min | max | res | scale |
|---|---|---|---|---|
| $P_{A1}$ (bar) | 0 | 2 | 21 | lin |
| $P_{A2}$ (bar) | 0 | 2 | 21 | lin |
| $f_1$ (kHz) | 20 | 2000 | 101 | log |
| $f_2$ (kHz) | 20 | 2000 | 101 | log |
| $\theta$ (-) | 0 | $2\pi(1-1/20)$ | 20 | lin |
| $R_E$ ($\mu$m) | 1 | 10 | 21 | lin |

## 4. The numerical procedure

The integration procedure is as follows. At each parameter combination, the integration is started from the equilibrium condition $y_1(0) = 1$ and $y_2(0) = 0$. Thus, the co-existence of attractors is not examined as only one initial condition is applied. The first integration phase is stopped at the first local maximum $y_{1,1}^{max}$ of the dimensionless bubble radius $y_1$. The subsequent integration phases are performed from a local maximum $y_{1,n}^{max}$ to the next local maximum $y_{1,n+1}^{max}$, see also Fig. 1. The first 512 integration phases are regarded as initial transients and discarded. The properties of the next 64 integration phases are recorded: the local maxima $y_{1,n}^{max}$, the subsequent minimum bubble radii $y_{1,n}^{min}$ and the elapsed times between $y_{1,n}^{max}$ and $y_{1,n}^{min}$ denoted by $\tau_{c,n}$. The dynamics between the local maximum and the subsequent minimum radius is called a collapse phase throughout the paper, even if the pressure amplitudes are so small that the bubble is chemically inactive near the minimum radius. The saved properties of 64 collapses at a single parameter set allow one to perform a statistical analysis as well. Storing data of multiple subsequent collapses are important as a solution can be chaotic, quasiperiodic or periodic with high periodicity. Moreover, many smaller collapses called afterbounces can occur in a single period of the driving after a strong collapse. Thus, recording the property of a single collapse after the transient cannot represent the complex dynamics. This shall be important in the future to investigate the collapse rate (the number of strong collapses in unit time). The present paper focuses only on the strongest recorded collapse at each parameter set.

For further investigation, it is important to define a suitable expression to characterise the strength of a collapse. In the literature, many possibilities are available: expansion

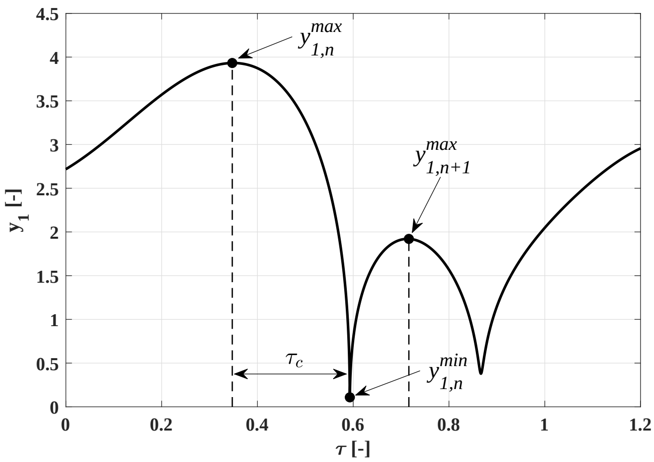


Figure 1: A typical time series of a dimensionless bubble radius $y_1$ show collapses. The characteristic quantities of the first collapse are also presented by the arrows.

ratio $R_{max}/R_E = y_1^{max}$ [38, 42, 60, 61, 80], compression ratio $R_{max}/R_{min} = y_1^{max}/y_1^{min}$ that is related to the maximum temperature of the bubble [42, 81], the quantity of $R_{max}^3/t_c$ [39, 41, 82] or the relative expansion $(R_{max} - R_E)/R_E = y_1^{max} - 1$ commonly used in numerical studies to characterise the magnitude of the oscillation [57, 62, 63]. Out of the many possibilities we choose the relative expansion

$$RE = \frac{R_{max} - R_E}{R_E} = y_1^{max} - 1 \tag{25}$$

that takes the different values

$$RE_n = \frac{R_{max,n} - R_E}{R_E} = y_{1,n}^{max} - 1 \tag{26}$$

in the course of the oscillation. Our already mentioned numerical investigation, including chemical kinetics, has revealed that *this quantity has the best correlation with the chemical yield* of a bubble [83]. It is widely accepted in the literature that inertial or transient cavitation occurs if the expansion ratio is approximately $R_{max}/R_E = y_1^{max} > 2$; that is, if the relative expansion is $RE > 1$ [38, 84–86]. In this way, the active cavitation threshold can be given *in terms of the relative expansion* denoted by $RE^{thr}$. According to our aforementioned study [83], the chemical yield of a bubble is a smooth, power-like function of the relative expansion $RE$. Therefore, any given threshold value for the chemical activity must be somewhat arbitrary. The results showed that the chemical activity starts to increase rapidly somewhere between $RE = 2$ and 3. Throughout this paper, these threshold values are investigated in detail denoted by $RE^{thr,2}$ and $RE^{thr,3}$, and the synergetic effect of the dual-frequency driving is explained in terms of these thresholds. It must be stressed that the term *active cavitation threshold* is used as a synonym to the inception of chemical activity in this paper. The detailed discussion of the "classic" terminology of inertial/transient cavitation (and their threshold values) is beyond the scope of the present study.

## 5. Definition of the active cavitation threshold in terms of the pressure amplitude for dual-frequency driving

The definition of the active cavitation threshold in terms of the relative expansion $RE^{thr}$ is very powerful as one can estimate the incidence of the chemical activity merely by inspecting the time series of the bubble radius. However, such a threshold can be defined also in terms of the input power $I$; that is, the minimum power required for chemical activity. In case of a single transducer, the generated pressure amplitude $P_A$ is proportional to the square root of the input power: $P_A \propto \sqrt{2I\rho_L c_L}$ [39, 80]. Therefore, the active cavitation threshold can be formulated also *in terms of the pressure amplitudes* by $P_A^{thr} = P_A^{opt}$, where $P_A^{opt}$ denotes the minimum pressure amplitude required for chemical activity with single frequency driving. The generalisation for a dual-frequency case can be written as

$$P_A^{thr} = \sqrt{(P_{A1}^{opt})^2 + (P_{A2}^{opt})^2}, \tag{27}$$

taking into account the relationship between the input power and the generated pressure amplitude. Here, $P_A^{thr}$ is an equivalent pressure amplitude of a single frequency driving having the same input power as the sum of the input powers of the individual frequency components in the dual-frequency case.

To determine a suitable threshold for the pressure amplitude, information about the collapse strength is still necessary. In this sense, $P_A^{thr,2}$ and $P_A^{thr,3}$ mean the minimum (equivalent) pressure amplitudes required to reach $RE^{thr,2}$ and $RE^{thr,3}$, respectively, which are the necessary collapse strengths for chemical activity, see the discussion in Sec. 4. The procedure to determine $P_{A1}^{opt}$ and $P_{A2}^{opt}$ is demonstrated in Fig. 2 for frequencies $f_1 = 200\,\mathrm{kHz}$, $f_2 = 34.76\,\mathrm{kHz}$, phase shift $\theta = 0$ and for bubble size $R_E = 10\,\mu\mathrm{m}$. In the figure, the colour code is the maximum achievable relative expansion $RE_n^{max}$ plotted as a function of the pressure amplitudes $P_{A1}$ and $P_{A2}$. The active cavitation threshold $RE^{thr,2}$ is denoted by the black curve. According to Eq. (27), the pressure amplitude combinations having the same total input power can be represented by circles. The larger the radius of the circle the larger the total input power. The optimal choice of the amplitude pair on the black threshold line corresponds to the circle having the lowest radius (minimal input power). This is demonstrated by the red circle, and the related amplitude pair $P_{A1}^{opt}$ and $P_{A2}^{opt}$ is marked by the green dot. In this way, for every combination of $f_1$, $f_2$, $\theta$ and $R_E$, values of $P_A^{thr,2}$ and $P_A^{thr,3}$ can be associated. Observe that with the help of the active cavitation threshold in terms of the pressure amplitudes, the investigated parameter space is reduced to four dimensions.

## 6. Optimal parameter combination to minimise $P_A^{thr,2}$

Figure 3 summarises the values of the active cavitation threshold $P_A^{thr,2}$ as a function of the frequencies $f_1$ and $f_2$ between 20 kHz and 2 MHz at different bubble sizes $R_E$. The first, second, third and fourth rows of the subpanels are related to $R_E = 2\,\mu\mathrm{m}$, $4\,\mu\mathrm{m}$, $6\,\mu\mathrm{m}$ and $10\,\mu\mathrm{m}$ bubble sizes, respectively. The phase shift between the harmonic components of the driving is kept constant $\theta = 0$. Keep in mind that the lower the value of $P_A^{thr,2}$ the lower the required input energy for chemically active cavitation. In the first column of the subpanels, the range of $P_A^{thr,2}$ is kept constant between 0.5 bar and 1.5 bar

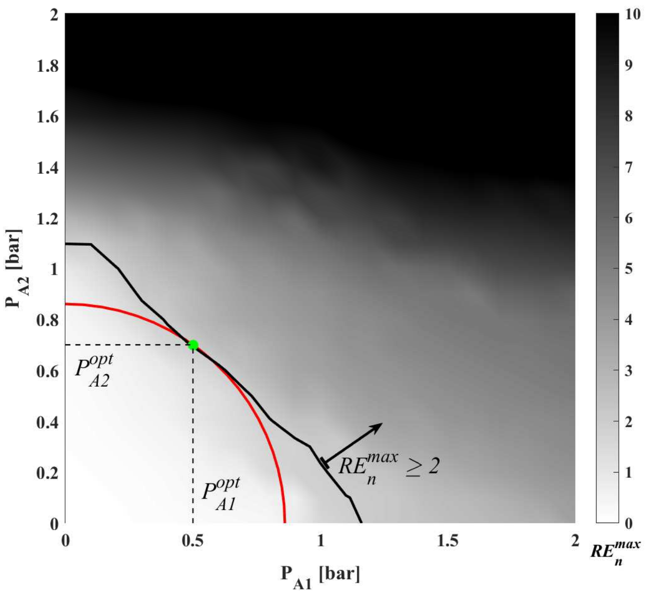


Figure 2: The determination of the active cavitation threshold in terms of the pressure amplitude for dual-frequency driving.

for a better comparison of the effect of the bubble size $R_E$. In the second column, the ranges are adjusted so that the location of the minima of $P_A^{thr,2}$ can be clearly identified.

From the increasing tendency of the adjusted ranges in the second column of Fig. 3, it is clear that the active cavitation threshold $P_A^{thr,2}$ increases with decreasing bubble size. The reason is the higher value of Blake's critical threshold [87] for smaller bubbles. In addition, three main regions can be identified for local/global minima of $P_A^{thr,2}$. The first region is related to the main resonance of the system and denoted by I, see Fig. 3E. The main resonance appear as vertical and horizontal stripes in the frequency plane $(f_1, f_2)$ whose locations are bubble size-dependent according to the linear eigenfrequency of the system [14, 88]:

$$f_0 = \frac{1}{2\pi}\sqrt{\frac{3\gamma(P_\infty - p_V)}{\rho_L R_E^2} - \frac{2(3\gamma-1)\sigma}{\rho_L R_E^3}}. \tag{28}$$

The second region, marked by II in Fig. 3E, is the well-known giant response [14] region located always in the lowest frequency domain. Due to the low frequency, the bubble has enough time to grow large (several times higher than its equilibrium size) resulting in a very strong collapse afterwards. The third region is a local minimum of $P_A^{thr,2}$ that occurs at the diagonal of the frequency plane (denoted by III). Because of the equal frequencies, this case represents single frequency driven bubbles and thus, it highlights the fact that to produce a certain pressure amplitude, it is more energy-efficient to use two transducers with half amplitudes.

For simplicity, the aforementioned regions are marked only in subpanel Fig. 3E. However, all or some of them are present also at other bubble sizes. For small bubbles, case II, the giant response region dominates the frequency plane. In contrast, for large bub-

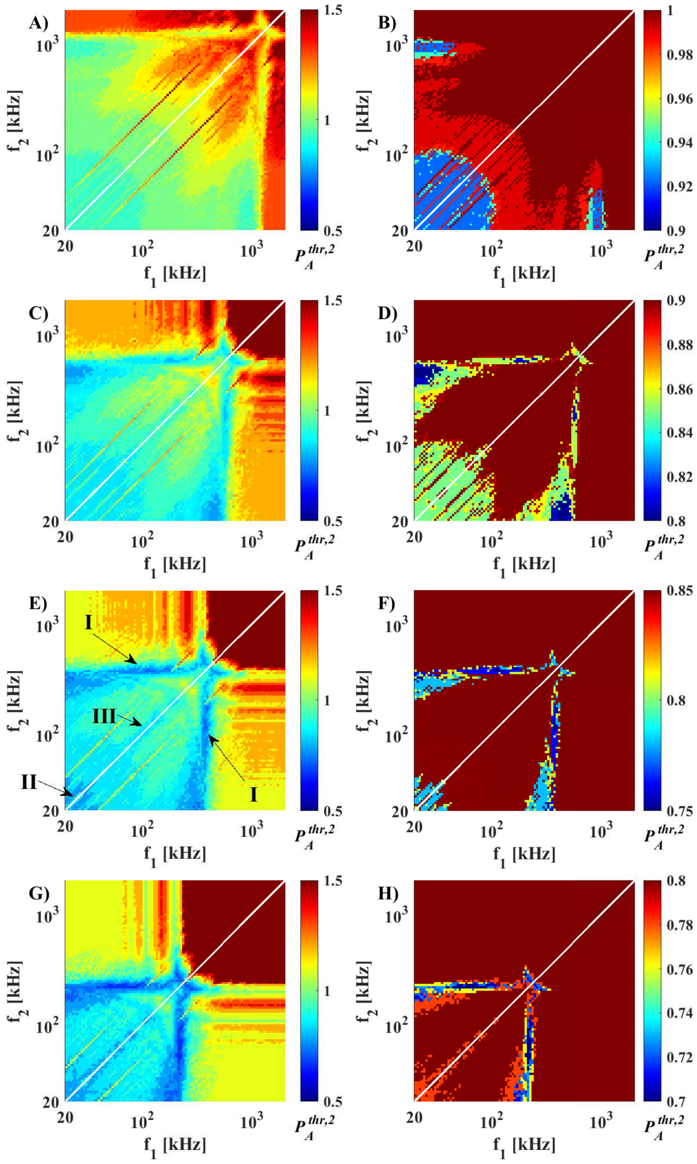


Figure 3: The dual-frequency active cavitation threshold $P_A^{thr,2}$ (in bar) as a function of the frequencies $f_1$ and $f_2$ in the range 20 kHz to 2 MHz at different bubble sizes $R_E$. The phase shift $\theta = 0$ is constant. The first, second, third and fourth rows of the subpanels are computed at $R_E = 2\,\mu$m, $4\,\mu$m, $6\,\mu$m and $10\,\mu$m bubble sizes, respectively.

bles, case I, the main resonance dominates the frequency plane. Between large and small bubbles, there is a somewhat smooth transition from case I to case II or vice versa. Case III never dominates the $(f_1, f_2)$ plane. It is worth mentioning that case II, the giant response, can be regarded as a sub-region of case III (equal frequencies). However, we keep the distinction to emphasize the application of small frequencies that generates the giant response.

Before proceeding further, it is important to discuss the effect of the phase shift $\theta$. To clearly identify the role of $\theta$, an animation has been created where the panels similar to the ones shown in the first column of Fig. 3 are presented as a function of all the investigated bubble sizes $R_E$ and phase shifts $\theta$. These are changing with time. At fixed bubble sizes, the figures related to different values of $\theta$ are almost identical. Therefore, for single spherical bubbles, its effect on the active cavitation threshold can be neglected. The animation is available as supplementary material called EffectOfTheta_Animation.avi.

The remaining task is to represent the optimal setup of the frequency pairs (minimum $P_A^{thr,2}$) as a function of the bubble size $R_E$. Therefore, for each bubble sizes, the frequencies $f_1$ and $f_2$ are extracted from the location of the global minimum of $P_A^{thr,2}$. The corresponding pressure amplitudes $P_{A1}^{opt}$ and $P_{A2}^{opt}$ are also registered to have information about the pressure amplitude distribution between the two frequency components. The results are summarised in Fig. 4. Keep in mind that simulations are carried out with a fine resolution of the bubble size, and Fig. 3 represents only some typical cases. The red line in the top panel of Fig. 4 is the resonance frequency of the bubbles calculated via Eq. (28). The red dots in the bottom panel are the lowest possible values of the active cavitation threshold $P_A^{thr,2}$ at a given bubble size, the corresponding frequencies and amplitudes are marked by the green and blue crosses, respectively (in both panels).

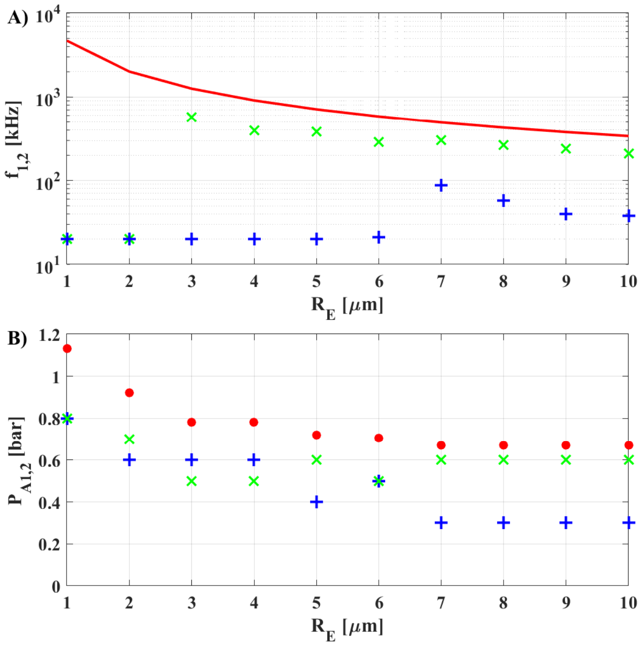


Figure 4: The optimal values of the driving frequencies (panel A) and the pressure amplitudes (panel B) for active cavitation threshold $P_A^{thr,2}$. They are denoted by the blue and green crosses. The red line in panel A) is the size-dependent linear resonance frequency of the bubble. The red dots in panel B) represent the lowest values of $P_A^{thr,2}$.

The condensed representation of the results in Fig. 4 supports our previous observations. For small bubble radii, approximately below 3 $\mu$m, the giant response region is the optimal choice with equal frequencies (single frequency driving) and equal pressure amplitudes (energy efficiency). For large bubbles, above 6 $\mu$m, it is important to drive the system nearly at its resonance frequency, see the green crosses in the upper panel. The deviation between the red curve and the green crosses is due to the highly non-linear nature of the bubble dynamics [84, 89–104]. The pressure amplitude of the second frequency component is much smaller (compare the blue crosses in both panels); thus, the main resonance frequency is the dominant component and it plays the major role here. For moderate bubble sizes, between 3 $\mu$m and 6 $\mu$m, both the giant response (lowest frequency, here 20 kHz) and the main resonance (close to the red curve in the upper panel) are important for an optimal setup. Observe that the amplitudes are nearly equal in this regime; thus, both frequency components are important. This setup can be observed as a relatively big blue region in Fig. 3D located at the low-high frequency combinations. Since this bubble size region covers the majority of the experimentally observed bubble size distribution [76–79], this finding can be a possible explanation for the synergetic effect of dual-frequency driving using a low-high frequency combination.

## 7. Optimal parameter combination to minimise $P_A^{thr,3}$

Although the value of the relative expansion $RE = 2$ ($RE^{thr,2}$) is an accepted measure for the incidence of chemical activity, some reactions needs much higher collapse strength to have measurable effects (e.g. nitrogen dissociation [19, 105]). Therefore, the evaluation process presented in the previous section (Sec. 6), is repeated for $RE = 3$ ($RE^{thr,3}$). The corresponding active cavitation threshold in terms of the equivalent pressure amplitude is denoted by $P_A^{thr,3}$. The condensed summary of the results is shown in Fig. 5. The colour code is the same as in case of Fig. 4. The message of the diagram is clear: use small frequencies (giant response) and use equal frequencies with equal amplitudes (energy efficiency). *That is, the giant response always dominates the frequency parameter plane regardless of the bubble size.* Similarly, as in case of $P_A^{thr,2}$, the effect of the phase shift $\theta$ is negligible. It is worth mentioning already here that giant response is not a speciality for dual-frequency driving. Therefore, a synergetic effect cannot be recognised in Fig. 5, only energy efficiency. For a detailed discussion see Sec. 8.

## 8. Discussion

Dual-frequency driving can be an energy-efficient technique for enhancing the yield in sonochemical applications. The upper bound of the peak value of the pressure amplitude that can be generated is the sum of the amplitudes of the harmonic components

$$P_A \leq P_{A1} + P_{A2} \tag{29}$$

expressing the superposition of the generated pressure waves. Therefore, using two transducers with the same frequencies and amplitudes, and with zero phase difference, one can reduce energy consumption by a factor of two to generate the same amplitude:

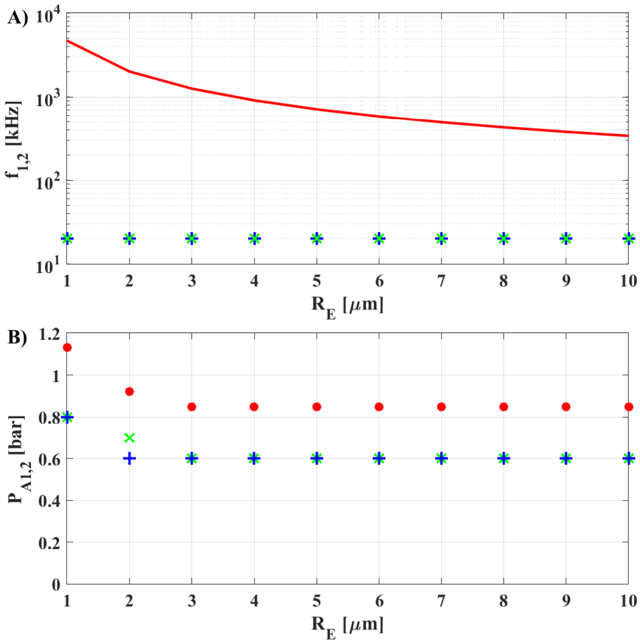


Figure 5: The optimal values of the driving frequencies (panel A) and the pressure amplitudes (panel B) for active cavitation threshold $P_A^{thr,3}$. They are denoted by the blue and green crosses. The red line in panel A) is the size-dependent linear resonance frequency of the bubble. The red dots in panel B) represent the lowest values of $P_A^{thr,3}$.

$$
\begin{aligned}
I_{SF} &\propto P_A^2 \\
I_{DF} &\propto P_{A1}^2 + P_{A2}^2 \\
&= (0.5P_A)^2 + (0.5P_A)^2 \\
&= 0.25P_A^2 + 0.25P_A^2 \\
&= 0.5P_A^2,
\end{aligned}
\tag{30}
$$

where $I_{SF}$ and $I_{DF}$ are the input powers for the single and dual-frequency driving, respectively. However, this observation cannot be regarded as a synergetic effect, it is purely an energy efficiency consideration of ultrasonic transducers.

A real synergetic effect can be observed for active cavitation threshold $RE^{thr,2}$ between bubble sizes $3\,\mu$m and $6\,\mu$m, where the application of a low and a high-frequency combination yields the lowest required power to reach the active cavitation threshold. The synergy is the mixture of the giant response (low frequency) and the main resonance (high frequency) phenomena. It is demonstrated through an example in Fig. 6 for a bubble size of $5\,\mu$m. According to Fig. 4, the optimal dual-frequency setup is $P_{A1} = 0.6$ bar with $f_1 = 370$ kHz and $P_{A2} = 0.4$ bar with $f_1 = 20$ kHz. From Fig. 6A-B, it is clear that applying the harmonic components separately, the maximum expansion of the bubble is far from the threshold value $RE^{thr,2}$ (red horizontal line at $y_1 = 3$). The dual-frequency signal is presented in Fig. 6E. Observe that how its peak value can be estimated by the addition of the pressure amplitudes $P_{A1}$ and $P_{A2}$, see also Eq. (29). In Fig. 6C-D, single frequency driven cases are demonstrated employing an increased amplitude of $P_A = 1$ bar that is the peak value of the dual-frequency signal. In this way, the effect of the applications of two transducers can be simulated using the same frequencies at amplitudes $P_{A1} = 0.6$ bar and $P_{A2} = 0.4$ bar. The maximum bubble expansions are still far away from the active cavitation threshold. However, with the same pressure amplitudes (same input power) but with a mixture of frequencies, the maximum bubble expansion can be increased significantly, see Fig. 6F. It reaches the active cavitation threshold as it is expected. It must be stressed that such a synergetic effect is hard to find by trial and error due to the high dimensional parameter space. This justifies the application of high-performance GPU computing. Interestingly, many experimental studies reported the synergetic effect of the application of low-high frequency combination using similar frequency combinations, see Refs. [37, 42, 44]. This justifies that the aforementioned phenomenon can be a possible explanation for the synergy.

Increasing the active cavitation threshold form $RE^{thr,2}$ to $RE^{thr,3}$, the above-described synergetic effect completely disappears. The optimal choice is to use the lowest frequencies (20 kHz) for both harmonic components, and use equal amplitudes. This setup represents the energy-efficient exploitation of the giant response phenomenon observed at low-frequency driving. This finding puts to the question of the above demonstrated synergetic effect since the chemical activity increases rapidly with increasing relative expansion $RE$ (the threshold values $RE^{thr,2}/RE^{thr,3}$ are only estimates for the incidence of the chemical activity). For instance, the production of $OH^-$ radical is approximately $4 \times 10^5$, $3 \times 10^6$ and $7 \times 10^7$ molecules during a single collapse for relative expansions $RE = 2$, 3 and 6, respectively [83]. In this sense, for high chemical yield, the best option is always the generation of giant response without involving and exploiting the main resonance.

The study Ref. [83] is carried out with an oxygen bubble placed in water. Even in such a simple configuration, the number of the chemical species is 9 and the number of reaction equations is 44. The different reaction equations are activated at different temperature values; thus, for different collapse strengths, the composition of the chemical products of a bubble can be quite different as well. Therefore, an optimal collapse strength (peak temperature) can exist according to the requirements of the chemical output. This is reported by Yasui et al. [105] with nitrogen bubbles in water, where the production of free radicals decreases with the peak temperature above an optimal value. The reason is that at very high temperature, the nitrogen molecules can dissociate; thus, reaction equations related to nitrogen atoms can play a significant role and consume the free radicals. In conclusion, for every liquid-gas composition, an optimal temperature and collapse strength might be associated depending on the required chemical yield. Therefore, the above-described synergetic effect can be important if the optimal collapse strength in terms of the relative expansion is approximately below $RE = 3$.

As a final remark, it is very likely that the synergetic effect cannot be explained by a single phenomenon, i.e., by the active cavitation threshold in terms of the pressure amplitude only as it is studied in the present paper. The correct treatment is to take into account the chemical kinetics in the bubble model and compute the production of the required chemical species directly. However, such a computation needs orders of magnitude larger computational resources as the number of the parameters is still

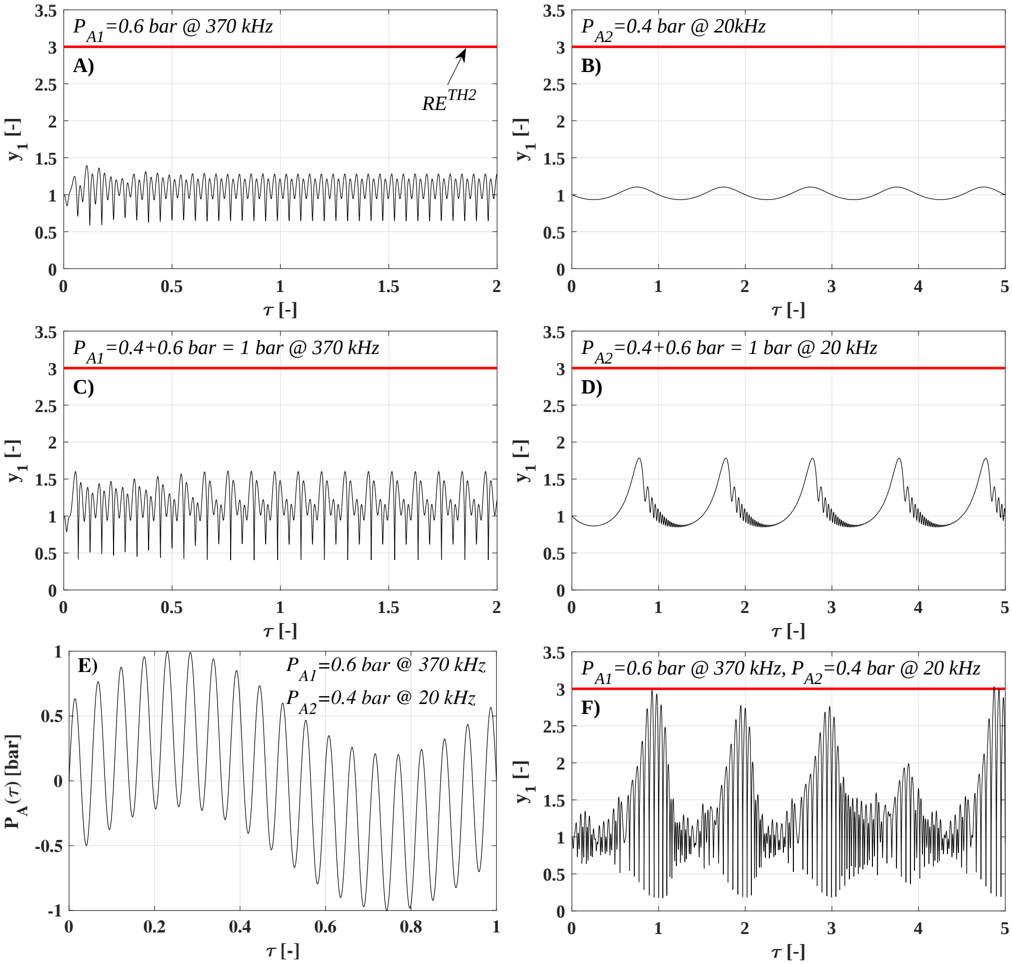


Figure 6: Synergetic effect of dual-frequency driving at a bubble size of $5\,\mu$m. Panel A and C: time series of the bubble radius of single frequency driving with 370 kHz at different pressure amplitudes $P_{A1} = 0.6$ bar and $P_{A1} = 1$ bar. Panel B and D: time series of the bubble radius of single frequency driving with 20 kHz at different pressure amplitudes $P_{A2} = 0.4$ bar and $P_{A2} = 1$ bar. Panel E and F: driving signal and time series of the bubble radius of the dual-frequency driving. The pressure amplitudes are $P_{A1} = 0.6$ bar and $P_{A2} = 0.4$ bar with frequencies $f_1 = 370$ kHz and $f_2 = 20$ kHz.

high but the complexity of the model increases significantly. In addition, other physical phenomena can also play an important role, for instance, the collapse rate (number of strong collapses in a unit time), spherical stability [91, 106–112] (efficient mixing of the bubble interior with the liquid [24]) or rectified diffusion [113–115] (faster growth of the bubbles to a chemically active state [65]). The study of these effects is in the main focus of our forthcoming papers. Moreover, the dual-frequency driving can have significant influence on the dynamics of a bubble cluster, the size distribution of the bubbles, the nucleation procedure or the structure of the clusters via the secondary Bjerknes forces. These latter effects are already discussed in Sec. 1.

## 9. Summary

A dual-frequency driven single spherical bubble was studied numerically. The model employed was the Keller–Miksis oscillator that is a non-linear second-order ordinary differential equation. The main aim was to provide a theoretical background for the synergetic effect of dual-frequency driving in terms of the active cavitation threshold. The investigated parameter space was composed by the pressure amplitudes, frequencies, phase shift between the two harmonic components and the bubble size. Even with the moderate resolution of the 6-dimensional parameter space, the total number of the simulated parameter combinations was approximately 2 billion. Therefore, the high processing power of GPUs was exploited to obtain the results within a reasonable time. The evaluation of the results showed that for an active cavitation threshold (in terms of relative expansion) lower than approximately $(R_{max} - R_E)/R_E = 3$, the application of low-frequency driving (giant response) combined with high-frequency component (main resonance) can significantly increase the collapse strength of a bubble; thus, it significantly lowers the required input power to generate chemically active bubbles. This synergetic effect holds for bubble sizes between $3\,\mu$m and $6\,\mu$m, which covers the range of the experimentally observed typical bubble size distribution in a bubble cluster. For a higher active cavitation threshold, above $(R_{max} - R_E)/R_E = 3$, the synergetic effect disappears and the giant response (low frequency) with equal pressure amplitude (energy efficiency) is always the optimal choice. Therefore, the aforementioned synergetic effect plays an important role only if the required collapse strength (induced peak temperature) is moderate for the optimal chemical yield.

## Acknowledgement

This paper was supported by the Alexander von Humboldt Foundation, by the János Bolyai Research Scholarship of the Hungarian Academy of Sciences, by the Deutsche Forschungsgemeinschaft (DFG) grant no. ME 1645/7-1, and by the Higher Education Excellence Program of the Ministry of Human Capacities in the frame of Water science & Disaster Prevention research area of Budapest University of Technology and Economics (BME FIKP-VÍZ).

## References

[1] B. D. Storey, A. J. Szeri, Water vapour, sonoluminescence and sonochemistry, Proc. R. Soc. Lond. A 456 (1999) (2000) 1685–1709.

[2] T. J. Mason, Some neglected or rejected paths in sonochemistry – A very personal view, Ultrason. Sonochem. 25 (2015) 89–93.

[3] F. Cavalieri, F. Chemat, K. Okitsu, A. Sambandam, K. Yasui, B. Zisu, Handbook of Ultrasonics and Sonochemistry, 1st Edition, 2016.

[4] R. J. Wood, J. Lee, M. J. Bussemaker, A parametric review of sonochemistry: Control and augmentation of sonochemical activity in aqueous solutions, Ultrason. Sonochem. 38 (2017) 351–370.

[5] K. S. Suslick, N. C. Eddingsaas, D. J. Flannigan, S. D. Hopkins, H. Xu, The chemical history of a bubble, Acc. Chem. Res. 51 (9) (2018) 2169–2178.

[6] R. J. Wood, J. Lee, M. J. Bussemaker, Combined effects of flow, surface stabilisation and salt concentration in aqueous solution to control and enhance sonoluminescence, Ultrason. Sonochem. 58 (2019) 104683.

[7] R. J. Wood, J. Lee, M. J. Bussemaker, Disparities between sonoluminescence, sonochemiluminescence and dosimetry with frequency variation under flow, Ultrason. Sonochem. 58 (2019) 104645.
[8] R. Mettin, S. Luther, C.-D. Ohl, W. Lauterborn, Acoustic cavitation structures and simulations by a particle model, Ultrason. Sonochem. 6 (1) (1999) 25–29.
[9] R. Mettin, S. Luther, C.-D. Ohl, W. Lauterborn, Bubble size distribution near a pressure antinode, J. Acoust. Soc. Am. 105 (2) (1999) 1075–1075.
[10] W. Lauterborn, C.-D. Ohl, Acoustic Cavitation and Multi Bubble Sonoluminescence, Springer Netherlands, Dordrecht, 1999, pp. 97–104.
[11] R. Mettin, Bubble structures in acoustic cavitation, in: Bubble and Particle Dynamics in Acoustic Fields: Modern Trends and Applications, Research Signpost, Trivandrum, Kerala, India, 2005.
[12] R. Mettin, From a single bubble to bubble structures in acoustic cavitation, in: Oscillations, Waves and Interactions: Sixty Years Drittes Physikalisches Institut ; a Festschrift, Universitätsverlag Göttingen, Göttingen, Germany, 2007.
[13] F. Reuter, R. Mettin, W. Lauterborn, Pressure fields and their effects in membrane cleaning applications, J. Acoust. Soc. Am. 123 (5) (2008) 3047–3047.
[14] W. Lauterborn, T. Kurz, Physics of bubble oscillations, Rep. Prog. Phys. 73 (10) (2010) 106501.
[15] J. Eisener, A. Lippert, T. Nowak, C. Cairós, F. Reuter, R. Mettin, Characterization of acoustic streaming beyond 100 MHz, Physics Procedia 70 (2015) 151–154.
[16] F. Reuter, S. Lauterborn, R. Mettin, W. Lauterborn, Membrane cleaning with ultrasonically driven bubbles, Ultrason. Sonochem. 37 (2017) 542–560.
[17] F. Reuter, S. Lesnik, K. Ayaz-Bustami, G. Brenner, R. Mettin, Bubble size measurements in different acoustic cavitation structures: Filaments, clusters, and the acoustically cavitated jet, Ultrason. Sonochem. 55 (2019) 383–394.
[18] D. Fuster, A review of models for bubble clusters in cavitating flows, Flow Turbul. Combust. 102 (3) (2019) 497–536.
[19] K. Yasui, T. Tuziuti, T. Kozuka, A. Towata, Y. Iida, Relationship between the bubble temperature and main oxidant created inside an air bubble under ultrasound, J. Chem. Phys. 127 (15) (2007) 154502.
[20] K. Yasui, T. Tuziuti, J. Lee, T. Kozuka, A. Towata, Y. Iida, The range of ambient radius for an active bubble in sonoluminescence and sonochemical reactions, J. Chem. Phys. 128 (18) (2008) 184705.
[21] D. F. Rivas, L. Stricker, A. G. Zijlstra, H. J. G. E. Gardeniers, D. Lohse, A. Prosperetti, Ultrasound artificially nucleated bubbles and their sonochemical radical production, Ultrason. Sonochem. 20 (1) (2013) 510–524.
[22] L. Stricker, D. Lohse, Radical production inside an acoustically driven microbubble, Ultrason. Sonochem. 21 (1) (2014) 336–345.
[23] S. Merouani, O. Hamdaoui, Y. Rezgui, M. Guemini, Computer simulation of chemical reactions occurring in collapsing acoustical bubble: dependence of free radicals production on operational conditions, Res. Chem. Intermediat. 41 (2) (2015) 881–897.
[24] R. Mettin, C. Cairós, A. Troia, Sonochemistry and bubble dynamics, Ultrason. Sonochem. 25 (2015) 24–30.
[25] S. Merouani, O. Hamdaoui, Y. Rezgui, M. Guemini, Mechanism of the sonochemical production of hydrogen, Int. J. Hydrog. Energy. 40 (11) (2015) 4056–4064.
[26] K. Kerboua, O. Hamdaoui, Sonochemical production of hydrogen: Enhancement by summed harmonics excitation, Chem. Phys. 519 (2019) 27–37.
[27] S. S. Rashwan, I. Dincer, A. Mohany, B. G. Pollet, The Sono-Hydro-Gen process (Ultrasound induced hydrogen production): Challenges and opportunities, Int. J. Hydrog. Energy. 44 (29) (2019) 14500–14526.
[28] M. H. Islam, O. S. Burheim, B. G. Pollet, Sonochemical and sonoelectrochemical production of hydrogen, Ultrason. Sonochem. 51 (2019) 533–555.
[29] P. Riesz, T. Kondo, Free radical formation induced by ultrasound and its biological implications, Free Radical Bio. Med. 13 (3) (1992) 247–270.
[30] K. Yasuda, T. Torii, K. Yasui, Y. Iida, T. Tuziuti, M. Nakamura, Y. Asakura, Enhancement of sonochemical reaction of terephthalate ion by superposition of ultrasonic fields of various frequencies, Ultrason. Sonochem 14 (6) (2007) 699–704.
[31] A. A. Pradhan, P. R. Gogate, Degradation of p-nitrophenol using acoustic cavitation and Fenton chemistry, J. Hazard. Mater. 173 (1) (2010) 517–522.
[32] S. Merouani, O. Hamdaoui, Y. Rezgui, M. Guemini, Sensitivity of free radicals production in acoustically driven bubble to the ultrasonic frequency and nature of dissolved gases, Ultrason.

Sonochem. 22 (2015) 41–50.
[33] A. Gedanken, Using sonochemistry for the fabrication of nanomaterials, Ultrason. Sonochem. 11 (2) (2004) 47–55.
[34] H. Xu, B. W. Zeiger, K. S. Suslick, Sonochemical synthesis of nanomaterials, Chem. Soc. Rev. 42 (7) (2013) 2555–2567.
[35] M. H. Islam, M. T. Y. Paul, O. S. Burheim, B. G. Pollet, Recent developments in the sonoelectrochemical synthesis of nanomaterials, Ultrason. Sonochem. 59 (2019) 104711.
[36] K.-i. Kawabata, S.-i. Umemura, Use of second-harmonic superimposition to induce chemical effects of ultrasound, J. Phys. Chem. 100 (48) (1996) 18784–18789.
[37] G. Iernetti, P. Ciuti, N. Dezhkunov, M. Reali, A. Francescutto, G. Johri, Enhancement of high-frequency acoustic cavitation effects by a low-frequency stimulation, Ultrasonics Sonochemistry 4 (3) (1997) 263–268.
[38] V. S. Moholkar, S. Rekveld, M. M. C. G. Warmoeskerken, Modeling of the acoustic pressure fields and the distribution of the cavitation phenomena in a dual frequency sonic processor, Ultrasonics 38 (1) (2000) 666–670.
[39] P. A. Tatake, A. B. Pandit, Modelling and experimental investigation into cavity dynamics and cavitational yield: influence of dual frequency ultrasound sources, Chem. Eng. Sci. 57 (22) (2002) 4987–4995.
[40] S. D. Sokka, T. P. Gauthier, K. Hynynen, Theoretical and experimental validation of a dual-frequency excitation method for spatial control of cavitation, Phys. Med. Biol. 50 (9) (2005) 2167–2179.
[41] P. M. Kanthale, P. R. Gogate, A. B. Pandit, Modeling aspects of dual frequency sonochemical reactors, Chem. Eng. J. 127 (1-3) (2007) 71–79.
[42] P. M. Kanthale, A. Brotchie, M. Ashokkumar, F. Grieser, Experimental and theoretical investigations on sonoluminescence under dual frequency conditions, Ultrason. Sonochem. 15 (4) (2008) 629–635.
[43] V. S. Moholkar, Mechanistic optimization of a dual frequency sonochemical reactor, Chem. Eng. Sci. 64 (24) (2009) 5255–5267.
[44] A. Brotchie, R. Mettin, F. Grieser, M. Ashokkumar, Cavitation activation by dual-frequency ultrasound and shock waves, Phys. Chem. Chem. Phys. 11 (2009) 10029–10034.
[45] D. Dellavale, L. Rechiman, J. M. Rosselló, F. J. Bonetto, Upscaling energy concentration in multifrequency single-bubble sonoluminescence with strongly degassed sulfuric acid, Phys. Rev. E 86 (2012) 016320.
[46] S. Khanna, S. Chakma, V. S. Moholkar, Phase diagrams for dual frequency sonic processors using organic liquid medium, Chem. Eng. Sci. 100 (2013) 137–144.
[47] J. M. Rosselló, D. Dellavale, F. J. Bonetto, Positional stability and radial dynamics of sonoluminescent bubbles under bi-harmonic driving: Effect of the high-frequency component and its relative phase, Ultrason. Sonochem. 31 (2016) 610–625.
[48] N. B. Waldo, C. D. Vecitis, Combined effects of phase-shift and power distribution on efficiency of dual-high-frequency sonochemistry, Ultrason. Sonochem. 41 (2018) 100–108.
[49] L. Carpenedo, P. Ciuti, A. Francescutto, G. Iernetti, G. K. Johri, Space-time interaction of two ultrasonic fields and sonoluminescence during transient cavitation in distilled water, Acoust. Lett. 10 (1987) 178–181.
[50] R. Feng, Y. Zhao, C. Zhu, T. J. Mason, Enhancement of ultrasonic cavitation yield by multi-frequency sonication, Ultrason. Sonochem. 9 (5) (2002) 231–236.
[51] P. Ciuti, N. V. Dezhkunov, A. Francescutto, A. I. Kulak, G. Iernetti, Cavitation activity stimulation by low frequency field pulses, Ultrason. Sonochem. 7 (4) (2000) 213–216.
[52] A. H. Barati, M. Mokhtari-Dizaji, H. Mozdarani, Z. Bathaie, Z. M. Hassan, Effect of exposure parameters on cavitation induced by low-level dual-frequency ultrasound, Ultrason. Sonochem. 14 (6) (2007) 783–789.
[53] M. Rahimi, S. Safari, M. Faryadi, N. Moradi, Experimental investigation on proper use of dual high-low frequency ultrasound waves—Advantage and disadvantage, Chem. Eng. Process. 78 (2014) 17–26.
[54] J. M. Rosselló, D. Dellavale, F. J. Bonetto, Energy concentration and positional stability of sonoluminescent bubbles in sulfuric acid for different static pressures, Phys. Rev. E 88 (3) (2013) 033026.
[55] Y. Zhang, S. Li, Acoustical scattering cross section of gas bubbles under dual-frequency acoustic excitation, Ultrason. Sonochem. 26 (2015) 437–444.
[56] Y. Zhang, Y. Zhang, S. Li, The secondary bjerknes force between two gas bubbles under dual-

frequency acoustic excitation, Ultrason. Sonochem. 29 (2016) 129–145.

[57] Y. Zhang, Y. Zhang, Chaotic oscillations of gas bubbles under dual-frequency acoustic excitation, Ultrason. Sonochem. 40 (2018) 151–157.

[58] K. Kerboua, O. Hamdaoui, Numerical investigation of the effect of dual frequency sonication on stable bubble dynamics, Ultrasonics Sonochemistry 49 (2018) 325–332.

[59] L. Ye, X. Zhu, Y. Liu, Numerical study on dual-frequency ultrasonic enhancing cavitation effect based on bubble dynamic evolution, Ultrason. Sonochem. 59 (2019) 104744.

[60] D. Suo, B. Govind, S. Zhang, Y. Jing, Numerical investigation of the inertial cavitation threshold under multi-frequency ultrasound, Ultrason. Sonochem. 41 (2018) 419–426.

[61] M. Wang, Y. Zhou, Numerical investigation of the inertial cavitation threshold by dual-frequency excitation in the fluid and tissue, Ultrason. Sonochem. 42 (2018) 327–338.

[62] Y. Zhang, Y. Zhang, S. Li, Combination and simultaneous resonances of gas bubbles oscillating in liquids under dual-frequency acoustic excitation, Ultrason. Sonochem. 35 (2017) 431–439.

[63] M. Guédra, C. Inserra, B. Gilles, Accompanying the frequency shift of the nonlinear resonance of a gas bubble using a dual-frequency excitation, Ultrason. Sonochem. 38 (2017) 298–305.

[64] Y. Zhang, X. Du, H. Xian, Y. Wu, Instability of interfaces of gas bubbles in liquids under acoustic excitation with dual frequency, Ultrason. Sonochem. 23 (2015) 16–20.

[65] Y. Zhang, D. Billson, S. Li, Influences of pressure amplitudes and frequencies of dual-frequency acoustic excitation on the mass transfer across interfaces of gas bubbles, Int. J. Heat Mass Transf. 66 (2015) 16–20.

[66] www.gpuode.com.

[67] https://github.com/ferenchegedus/massively-parallel-gpu-ode-solver.

[68] F. Hegedűs, MPGOS: GPU accelerated integrator for large number of independent ordinary differential equation systems, Budapest University of Technology and Economics, Budapest, Hungary (2019).

[69] H. Sasaki, J. Yasuda, R. Takagi, T. Miyashita, K. Goto, S. Yoshizawa, S. I. Umemura, Highly efficient cavitation-enhanced heating with dual-frequency ultrasound exposure in high-intensity focused ultrasound treatment, Jpn. J. Appl. Phys. 53 (7S) (2014) 07KF11.

[70] S. Umemura, K. Kawabata, K. Sasaki, Enhancement of sonodynamic tissue damage production by second-harmonic superimposition: theoretical analysis of its mechanism, IEEE Trans. Ultrason. Ferroelectr. Freq. Control 43 (6) (1996) 1054–1062.

[71] C. Shen, C. Cheng, C. Yeh, Phase-dependent dual-frequency contrast imaging at sub-harmonic frequency, IEEE Trans. Ultrason. Ferroelectr. Freq. Control 58 (2) (2011) 379–388.

[72] S. Chen, R. Kinnick, J. F. Greenleaf, M. Fatemi, Difference frequency and its harmonic emitted by microbubbles under dual frequency excitation, Ultrasonics 44 (2006) e123–e126.

[73] A. D. Phelps, T. G. Leighton, High-resolution bubble sizing through detection of the subharmonic response with a two-frequency excitation technique, J. Acoust. Soc. Am. 99 (4) (1996) 1985–1992.

[74] J. Holzfuss, M. Rüggeberg, R. Mettin, Boosting sonoluminescence, Phys. Rev. Lett. 81 (9) (1998) 1961–1964.

[75] S. Behnia, A. J. Sojahrood, W. Soltanpoor, O. Jahanbakhsh, Suppressing chaotic oscillations of a spherical cavitation bubble through applying a periodic perturbation, Ultrason. Sonochem. 16 (4) (2009) 502–511.

[76] F. Burdin, N. A. Tsochatzidis, P. Guiraud, A. M. Wilhelm, H. Delmas, Characterisation of the acoustic cavitation cloud by two laser techniques, Ultrason. Sonochem. 6 (1) (1999) 43–51.

[77] J. Lee, M. Ashokkumar, S. Kentish, F. Grieser, Determination of the size distribution of sonoluminescence bubbles in a pulsed acoustic field, J. Am. Chem. Soc. 127 (48) (2005) 16810–16811.

[78] A. Brotchie, F. Grieser, M. Ashokkumar, Effect of power and frequency on bubble-size distributions in acoustic cavitation, Phys. Rev. Lett. 102 (8) (2009) 084302.

[79] M. Ashokkumar, The characterization of acoustic cavitation bubbles – an overview, Ultrason. Sonochem. 18 (4) (2011) 864–872.

[80] A. V. Prabhu, P. R. Gogate, A. B. Pandit, Optimization of multiple-frequency sonochemical reactors, Chem. Eng. Sci. 59 (22) (2004) 4991–4998.

[81] P. Kanthale, M. Ashokkumar, F. Grieser, Sonoluminescence, sonochemistry ($H_2O_2$ yield) and bubble dynamics: Frequency and power effects, Ultrason. Sonochem. 15 (2) (2008) 143–150.

[82] M. Sivakumar, P. A. Tatake, A. B. Pandit, Kinetics of p-nitrophenol degradation: effect of reaction conditions and cavitational parameters for a multiple frequency system, Chem. Eng. J. 85 (2) (2002) 327–338.

[83] C. Kalmár, K. Klapcsik, F. Hegedűs, Relationship between the radial dynamics and the chemical production of a harmonically driven spherical bubble, Ultrason. Sonochem. submitted.

[84] A. J. Sojahrood, O. Falou, R. Earl, R. Karshafian, M. C. Kolios, Influence of the pressure-dependent resonance frequency on the bifurcation structure and backscattered pressure of ultrasound contrast agents: a numerical investigation, Nonlinear Dyn. 80 (1-2) (2015) 889–904.

[85] H. G. Flynn, C. C. Church, Transient pulsations of small gas bubbles in water, J. Acoust. Soc. Am. 84 (3) (1988) 985–998.

[86] R. E. Apfel, Some new results on cavitation threshold prediction and bubble dynamics, in: W. Lauterborn (Ed.), Cavitation and Inhomogeneities in Underwater Acoustics, Springer Berlin Heidelberg, Berlin, Heidelberg, 1980, pp. 79–83.

[87] F. G. Blake, The onset of cavitation in liquids, Tech. Rep. 12, Acoust. Res. Lab., Harvard Univ. (1949).

[88] C. E. Brennen, Cavitation and Bubble Dynamics, Oxford University Press, New York, 1995.

[89] W. Lauterborn, U. Parlitz, Methods of chaos physics and their application to acoustics, J. Acoust. Soc. Am. 84 (6) (1988) 1975–1993.

[90] U. Parlitz, V. Englisch, C. Scheffczyk, W. Lauterborn, Bifurcation structure of bubble oscillators, J. Acoust. Soc. Am. 88 (2) (1990) 1061–1077.

[91] P. Koch, T. Kurz, U. Parlitz, W. Lauterborn, Bubble dynamics in a standing sound field: The bubble habitat, J. Acoust. Soc. Am. 130 (5) (2011) 3370–3378.

[92] R. Varga, G. Paál, Numerical investigation of the strength of collapse of a harmonically excited bubble, Chaos Solitons Fract. 76 (2015) 56–71.

[93] A. J. Sojahrood, H. Haghi, R. Karshafian, M. C. Kolios, Numerical investigation of the nonlinear dynamics of interacting microbubbles, J. Acoust. Soc. Am. 140 (4) (2016) 3370–3370.

[94] R. Varga, F. Hegedűs, Classification of the bifurcation structure of a periodically driven gas bubble, Nonlinear Dynam. 86 (2) (2016) 1239–1248.

[95] F. Hegedűs, Topological analysis of the periodic structures in a harmonically driven bubble oscillator near Blake's critical threshold: Infinite sequence of two-sided Farey ordering trees, Phys. Lett. A 380 (9-10) (2016) 1012–1022.

[96] K. Klapcsik, F. Hegedűs, The effect of high viscosity on the evolution of the bifurcation set of a periodically excited gas bubble, Chaos Solitons Fract. 104 (17) (2017) 198–208.

[97] H. Haghi, A. J. Sojahrood, R. Karshafian, M. C. Kolios, Numerical investigation of the subharmonic response of a cloud of interacting microbubbles, J. Acoust. Soc. Am. 141 (5) (2017) 3493–3493.

[98] A. J. Sojahrood, Q. Li, H. Haghi, R. Karshafian, T. M. Porter, M. C. Kolios, Towards the accurate characterization of the shell parameters of microbubbles based on attenuation and sound speed measurements, J. Acoust. Soc. Am. 141 (5) (2017) 3493–3493.

[99] F. Hegedűs, W. Lauterborn, U. Parlitz, R. Mettin, Non-feedback technique to directly control multistability in nonlinear oscillators by dual-frequency driving, Nonlinear Dynam. 94 (1) (2018) 273–293.

[100] H. Haghi, A. J. Sojahrood, M. C. Kolios, On amplification of radial oscillations of microbubbles due to bubble-bubble interaction in polydisperse microbubble clusters under ultrasound excitation, J. Acoust. Soc. Am. 143 (3) (2018) 1862–1862.

[101] H. Haghi, A. J. Sojahrood, A. C. De Leon, A. Agata Exner, M. C. Kolios, Experimental and numerical investigation of backscattered signal strength from different concentrations of nanobubble and microbubble clusters, J. Acoust. Soc. Am. 144 (3) (2018) 1888–1888.

[102] A. J. Sojahrood, D. Wegierak, H. Haghi, R. Karshfian, M. C. Kolios, A simple method to analyze the super-harmonic and ultra-harmonic behavior of the acoustically excited bubble oscillator, Ultrason. Sonochem. 54 (2019) 99–109.

[103] C. A. MacDonald, V. Sboros, J. Gomatam, S. D. Pye, C. M. Moran, W. N. McDicken, A numerical investigation of the resonance of gas-filled microbubbles: resonance dependence on acoustic pressure amplitude, Ultrasonics 43 (2) (2004) 113–122.

[104] Y. Gong, M. Cabodi, T. M. Porter, Acoustic investigation of pressure-dependent resonance and shell elasticity of lipid-coated monodisperse microbubbles, Appl. Phys. Lett. 104 (7) (2014) 074103.

[105] K. Yasui, T. Tuziuti, Y. Iida, Optimum bubble temperature for the sonochemical production of oxidants, Ultrasonics 42 (1) (2004) 579–584.

[106] M. P. Brenner, D. Lohse, T. F. Dupont, Bubble shape oscillations and the onset of sonoluminescence, Phys. Rev. Lett. 75 (5) (1995) 954–957.

[107] A. A. Doinikov, Translational motion of a bubble undergoing shape oscillations, J. Fluid Mech. 501 (2004) 1–24.

[108] M. L. Calvisi, O. Lindau, J. R. Blake, A. J. Szeri, Shape stability and violent collapse of microbubbles in acoustic traveling waves, Phys. Fluids 19 (4) (2007) 047101.

[109] J. Holzfuss, Surface-wave instabilities, period doubling, and an approximate universal boundary of bubble stability at the upper threshold of sonoluminescence, Phys. Rev. E 77 (6) (2008) 066309.
[110] Y. Liu, M. L. Calvisi, Q. Wang, Nonlinear oscillation and interfacial stability of an encapsulated microbubble under dual-frequency ultrasound, Fluid Dyn. Res. 49 (2) 025518.
[111] J. M. Rosselló, W. Lauterborn, M. Koch, T. Wilken, T. Kurz, R. Mettin, Acoustically induced bubble jets, Phys. Fluids 30 (12) (2018) 122004.
[112] K. Klapcsik, F. Hegedűs, Study of non-spherical bubble oscillations under acoustic irradiation in viscous liquid, Ultrason. Sonochem. 54 (2019) 256–273.
[113] L. A. Crum, Acoustic cavitation series: part five rectified diffusion, Ultrasonics 2 (5) (1984) 215–223.
[114] L. A. Crum, Measurements of the growth of air bubbles by rectified diffusion, J. Acoust. Soc. Am 68 (1) (1980) 203–211.
[115] O. Louisnard, F. Gomez, Growth by rectified diffusion of strongly acoustically forced gas bubbles in nearly saturated liquids, Phys. Rev. E 67 (3) (2003) 036610.